

1 **Table of contents**

2

3 **SUPPLEMENTARY METHODS**

4 • Algorithm for χ -separation

5 • Implementation details of Monte-Carlo simulation

6 • Imaging parameters for MS lesion assessment

7 - Supplementary Figure 1

8

9 **SUPPLEMENTARY FIGURES**

10 • Supplementary Figures 2-10

11

12 **SUPPLEMENTARY NOTE**

13 • Proof of R_2' model in Eq. 4 for multiple susceptibility sources

14

15 **REFERENCES**

16

17

18

19 SUPPLEMENTARY METHODS

20 *Algorithm for χ -separation*

21 For the implementation of χ -separation, Eq. 5 is formulated as the following
 22 minimization problem:

$$\begin{aligned} \underset{\chi_{pos}, \chi_{neg}}{\operatorname{argmin}} \quad & \|W_r \cdot \{R_2' - (\overline{D_{r,pos}} \cdot |\chi_{pos}| + \overline{D_{r,neg}} \cdot |\chi_{neg}|)\} + i2\pi \cdot W_f \\ & \cdot \{f - D_f * (\chi_{pos} + \chi_{neg})\}\|_2^2 + \operatorname{reg}(\chi_{pos}, \chi_{neg}) \\ \text{subject to} \quad & \chi_{pos} \geq 0, \chi_{neg} \leq 0 \end{aligned}$$

23 where W_f is a weight accounting for the signal-to-noise ratio of the gradient echo signals¹,
 24 and W_r is a weight reducing the effects of unreliable R_2' :

$$W_r(\mathbf{r}) = \begin{cases} W_f(\mathbf{r})/10 & \text{where } R_2'(\mathbf{r}) > 30 \text{ Hz or } R_2'(\mathbf{r}) < 1 \text{ Hz,} \\ W_f(\mathbf{r}) & \text{otherwise.} \end{cases}$$

25 For the phantom data, the condition $R_2'(\mathbf{r}) < 1 \text{ Hz}$ was not applied in order to acquire
 26 signals from the agarose gel. The regularization term, $\operatorname{reg}(\chi_{pos}, \chi_{neg})$, is designed to reduce
 27 streaking artifacts in the results as suggested in the conventional QSM method².

$$\begin{aligned} \operatorname{reg}(\chi_{pos}, \chi_{neg}) \\ = 2 \cdot \lambda_1 \|M_{Mag}(\nabla \chi_{total})\|_1 + \lambda_1 \|M_{R_2'}(\nabla \chi_{pos})\|_1 + \lambda_1 \|M_{R_2'}(\nabla \chi_{neg})\|_1 \\ + \lambda_2 \|M_{CSF}(\chi_{pos} - \overline{\chi_{pos,CSF}})\|_2^2 + \lambda_2 \|M_{CSF}(\chi_{neg} - \overline{\chi_{neg,CSF}})\|_2^2 \end{aligned}$$

28 where λ_1 and λ_2 are regularization parameters, ∇ is a gradient operation, χ_{total} is a total
 29 susceptibility map calculated as the sum of χ_{pos} and χ_{neg} , M_{Mag} is a binary edge mask
 30 from magnitude¹, $M_{R_2'}$ is a binary edge mask from R_2' , M_{CSF} is a binary mask of
 31 ventricular cerebrospinal fluid², and $\overline{\chi_{\cdot,CSF}}$ is the mean positive (or negative) susceptibility
 32 in M_{CSF} ². All the other terms are the same as those in Eq. 5.

33 The minimization problem is solved iteratively using a conjugate gradient algorithm by
 34 simultaneously updating χ_{pos} and χ_{neg} in each iteration. If a susceptibility value violates
 35 the physical constraints (i.e., $\chi_{pos} \geq 0$ and $\chi_{neg} \leq 0$) during the iteration, it is forced to zero.
 36 The iteration stops when the residual, which is defined as $\|\chi_{n+1} - \chi_n\|_2 / \|\chi_n\|_2$ where χ_n

37 is the sum of χ_{pos} and χ_{neg} at the n^{th} iteration, is less than 0.01, or when it reaches 30
 38 iterations. The χ_{pos} and χ_{neg} maps are initialized as the solution of the following two
 39 linear equations:

$$40 \quad D_{r,pos}(\mathbf{r}) \cdot |\chi_{pos}(\mathbf{r})| + D_{r,neg}(\mathbf{r}) \cdot |\chi_{neg}(\mathbf{r})| = R_2'(\mathbf{r}),$$

$$41 \quad \chi_{pos} + \chi_{neg} = \chi_{conventional\ QSM}$$

42 where $\chi_{conventional\ QSM}$ is the reconstruction results of the conventional QSM².

43

44

Implementation details of Monte-Carlo simulation

To reduce the computational cost of the Monte-Carlo simulation, the number of the susceptibility sources was fixed to 10, while changing the voxel size of a segment to satisfy the susceptibility concentration. For example, a voxel size of $120 \times 120 \times 120 \mu\text{m}^3$ was used to achieve the susceptibility concentration of 0.0125 ppm while $83 \times 83 \times 83 \mu\text{m}^3$ was used for 0.0375 ppm. For the same reason, the protons were located only in the center slice. Then, the simulation results were appended along the z-direction, generating a 3D matrix (i.e., $26 \times 26 \times 32$). This matrix was used for the susceptibility reconstruction.

The convention of a magnetic dipole in Eq. 2 assumes no frequency shift at the origin based on the Lorentz sphere (i.e., $D_f(\mathbf{r} = \mathbf{0}) = 0$) (Wang and Liu, 2015). However, studies have reported that the non-zero frequency shift exists at the origin^{3,4}. This frequency shift was compensated for the simulation results⁴.

63 ***Imaging parameters for MS lesion assessment***

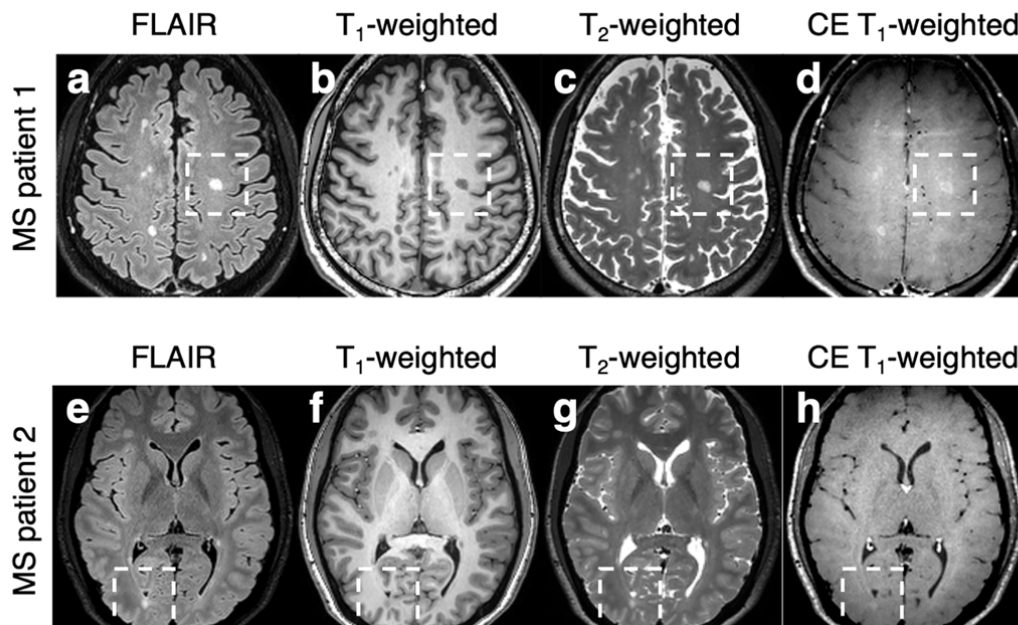
64 For the clinical assessment of MS lesions, the following four sequences were acquired in
65 the MS patients.

66 - FLAIR image: FOV = $256 \times 256 \times 180 \text{ mm}^3$, voxel size = $1 \times 1 \times 1 \text{ mm}^3$, TR = 4800 ms,
67 TE = 310 ms, bandwidth = 957 Hz/pixel, parallel imaging factor = 3×2 , inversion time
68 (TI) = 1650 ms, turbo factor = 167, refocusing angle = 30° , two averages, and total
69 acquisition time = 5.6 min.

70 - T₁-weighed image: FOV = $256 \times 256 \times 176 \text{ mm}^3$, voxel size = $1 \times 1 \times 1 \text{ mm}^3$, TR = 5851
71 ms, TE = 1599 ms, bandwidth = 191 Hz/pixel, flip angle = 7° , parallel imaging factor = 2,
72 TI = 1100 ms, turbo factor = 211, and total acquisition time = 5.4 min.

73 - T₂-weighed image: FOV = $240 \times 240 \times 188 \text{ mm}^3$, voxel size = $1 \times 1 \times 1 \text{ mm}^3$, TR = 2500
74 ms, TE = 300 ms, bandwidth = 609 Hz/pixel, parallel imaging factor = 2, turbo factor =
75 135, refocusing angle = 35° , and total acquisition time = 5.5 min.

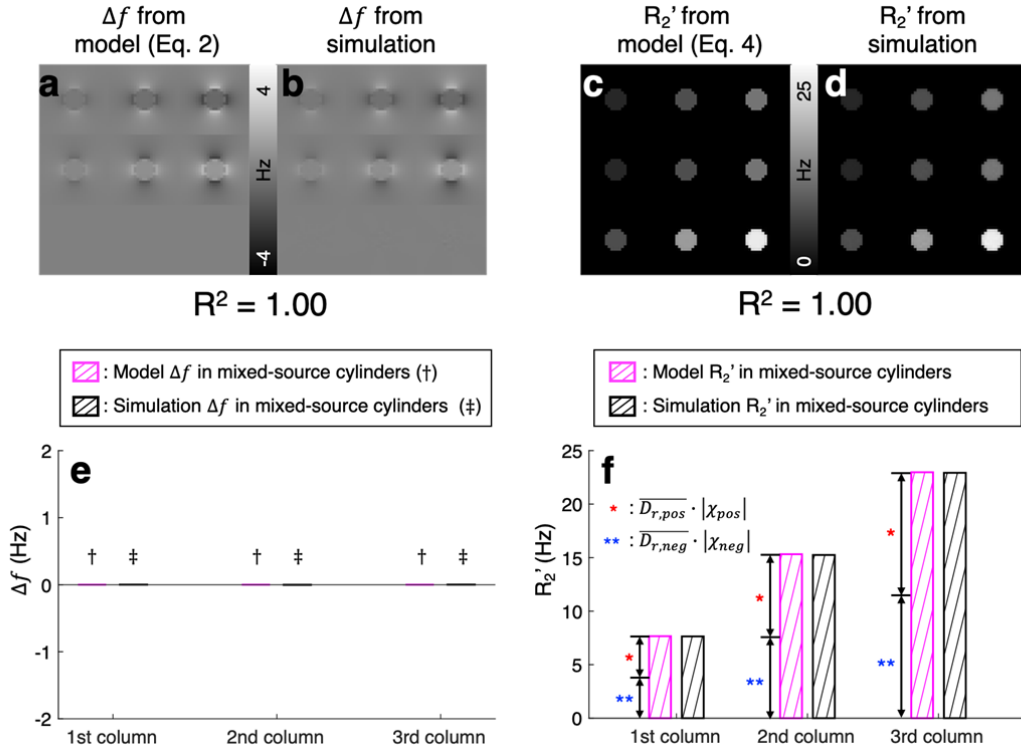
76 - CE T₁-weighed image: FOV = $240 \times 240 \times 180 \text{ mm}^3$, voxel size = $1 \times 1 \times 1 \text{ mm}^3$, TR =
77 500 ms, TE = 30 ms, bandwidth = 755 Hz/pixel, flip angle = 80° , TI = 1650 ms, turbo
78 factor = 30, refocusing angle = 35° , two averages, and total acquisition time = 3.9 min.



80 **Supplementary Figure 1. Images of the two MS patients (a-d from Patient 1; e-h from**
81 **Patient 2) for the clinical assessment of MS lesions. a and e, FLAIR images. b and f, T₁-**
82 **weighted images. c and g, T₂-weighted images. d and h, CE T₁-weighed images. White**
83 **boxes denote the areas of the MS lesions shown in Fig. 7.**

84

85



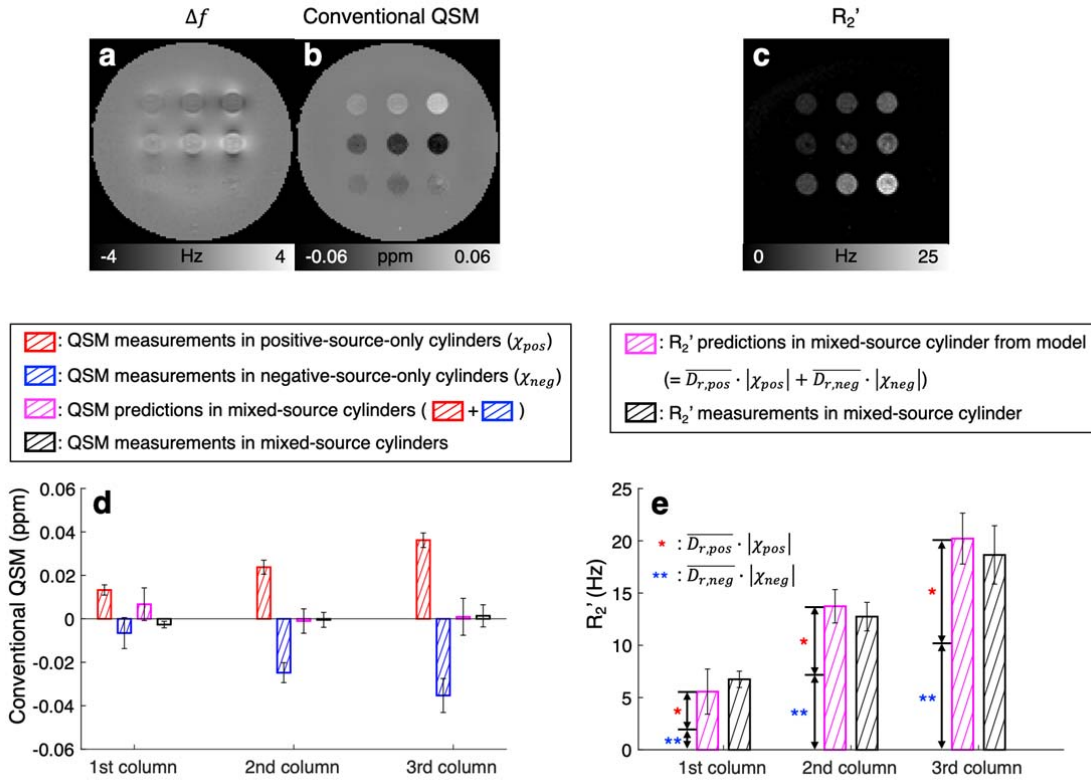
87

88 **Supplementary Figure 2. Validation of the proposed susceptibility models (Eqs. 2 and 4)**
 89 **using the Monte-Carlo simulation.** When the frequency shift maps from Eq. 2 are
 90 compared to those from the Monte-Carlo simulation, they reveal almost identical spatial
 91 distribution (**a-b**; $R^2 = 1.00$ in a voxel-wise linear regression). In particular, the simulation
 92 results of the mixed-source cylinders containing both positive and negative susceptibility
 93 sources (third row in **b**) report zero-frequency shifts, confirming our frequency shift model
 94 (Eq. 2), which states the signed sum of the positive and negative susceptibility determines the
 95 frequency shift. The quantitative frequency shift values of the mixed-source cylinders are
 96 shown in **e** with the pink and black bars representing the results from our model and the
 97 Monte-Carlo simulation, respectively (daggers and double daggers for the positions of the
 98 pink and black bars, respectively). In **c** and **d**, the R_2' results are summarized, demonstrating a
 99 strong correlation between our R_2' model in Eq. 4 and the simulation ($R^2 = 1.00$ in a voxel-
 100 wise linear regression). When the positive and negative susceptibility sources co-exist (third
 101 row in **d**), the R_2' values from the simulation are determined by the (weighted) absolute sum
 102 of the positive and negative susceptibility, validating our R_2' model in Eq. 4 (**f**). The single

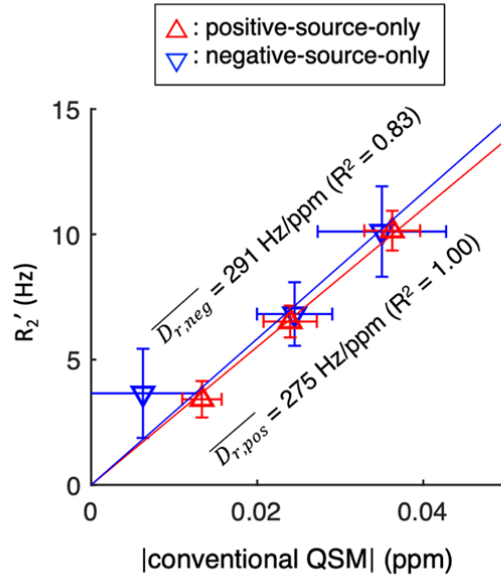
103 asterisk in \mathbf{f} denotes the portion of the positive susceptibility in R_2' from Eq. 4, whereas the
104 double asterisk denotes that of the negative susceptibility.

105

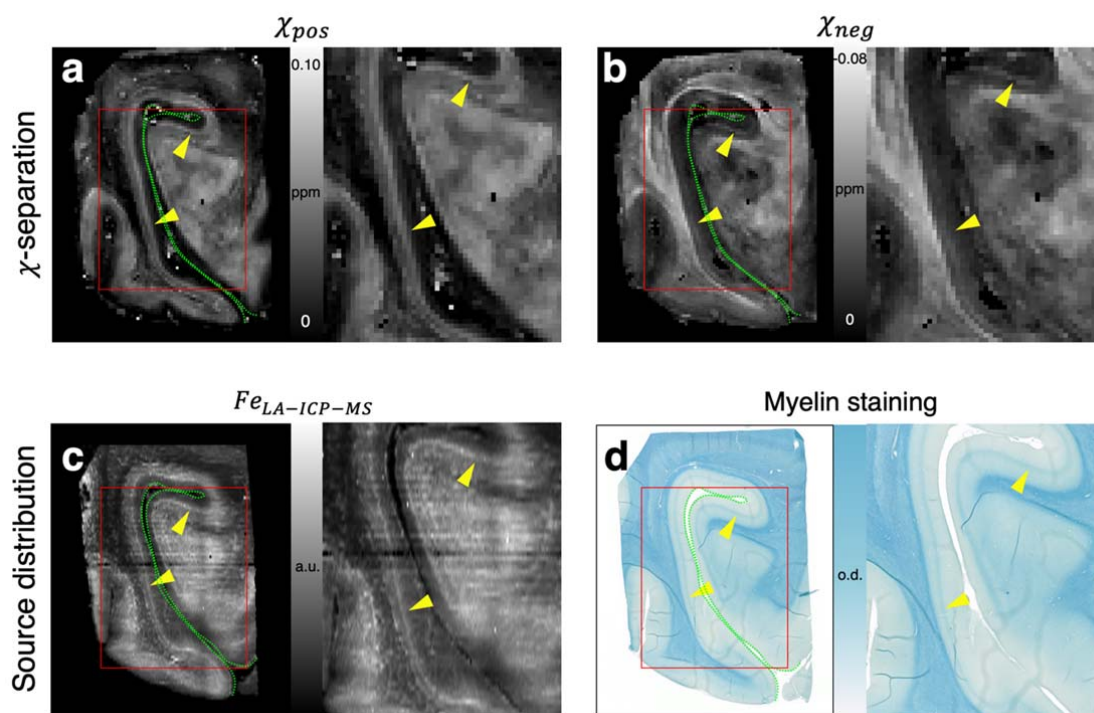
106



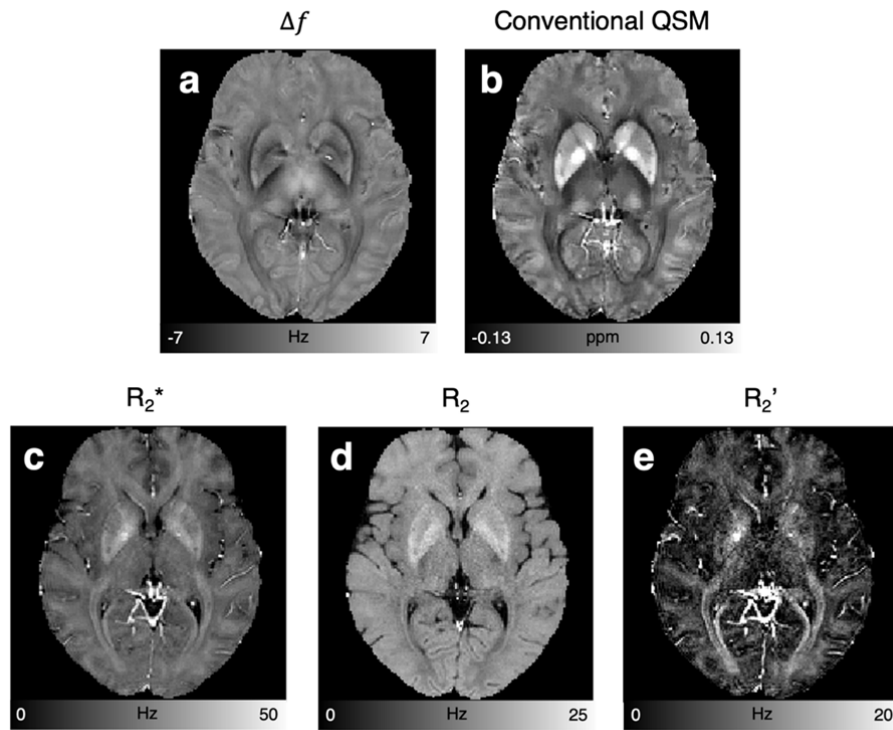
Supplementary Figure 3. Validation of the proposed susceptibility models (Eqs. 2 and 4) using the phantom experiment. **a**, Frequency shift map. **b**, QSM map. **c**, R_2' maps. For quantitative analysis, the QSM results are utilized instead of the frequency shift results because of the non-local effects from adjacent cylinders and background field in the frequency shift map. The bar graph (**d**; mean \pm standard deviation) reports the susceptibility concentrations of the positive-source-only cylinders (red bars) and the negative-source-only cylinders (blue bars). When the two measurements of each column are summed, they produced the QSM values in the pink bars. These measurements are close to the QSM values in the mixed-source cylinders (black bars) in all three columns. The results consolidate the validity of our model in Eq. 2. In the bar graph for R_2' (**e**; mean \pm standard deviation), the (weighted) absolute sums of the susceptibility measurements from the positive-source-only and negative-source-only cylinders (pink bars) match the R_2' values in the mixed-source cylinders (black bars). The single and double asterisks in **e** represent the portions of the positive and negative susceptibility sources, respectively. The results corroborate our model in Eq. 4.



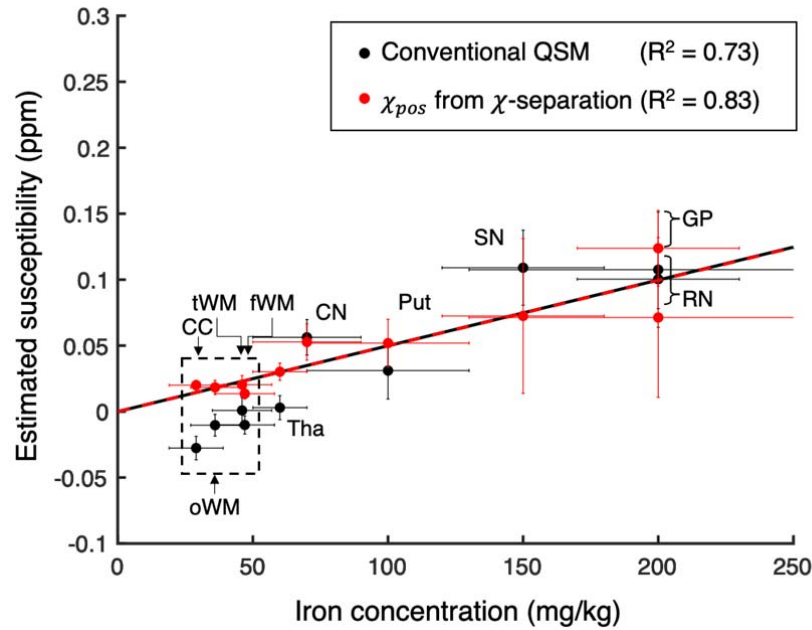
Supplementary Figure 4. Estimation of the relaxometric constants in the phantom experiment. The red upper triangles (or blue lower triangles) denote R_2' values with respect to the absolute values of the conventional QSM in the positive-source-only (or negative-source-only) cylinders. Error bars indicate the standard deviations. When a linear regression was performed for the positive susceptibility source measurements, the slope ($\overline{D_{r,pos}}$) was 275 Hz/ppm ($R^2 = 1.00$). For the negative susceptibility source measurements, the slope ($\overline{D_{r,neg}}$) was 291 Hz/ppm ($R^2 = 0.83$).



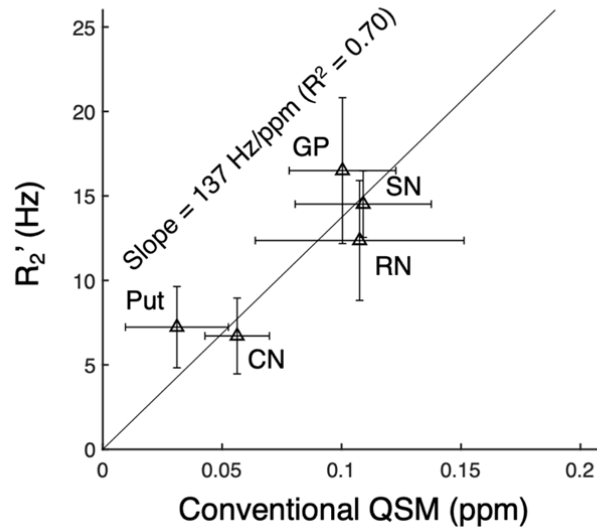
Supplementary Figure 5. Zoomed-in images of Figure 4. **a**, Positive susceptibility map. **b**, Negative susceptibility map. **c**, Iron image from LA-ICP-MS. **d**, Myelin image from LFB myelin staining. Red box areas, which contain the stria of Gennari (yellow arrows), are zoomed-in.



Supplementary Figure 6. MRI maps in the *in-vivo* brain. a, Frequency shift map. **b**, Conventional QSM map. **c**, R_2^* map. **d**, R_2 map. **e**, R_2' map.



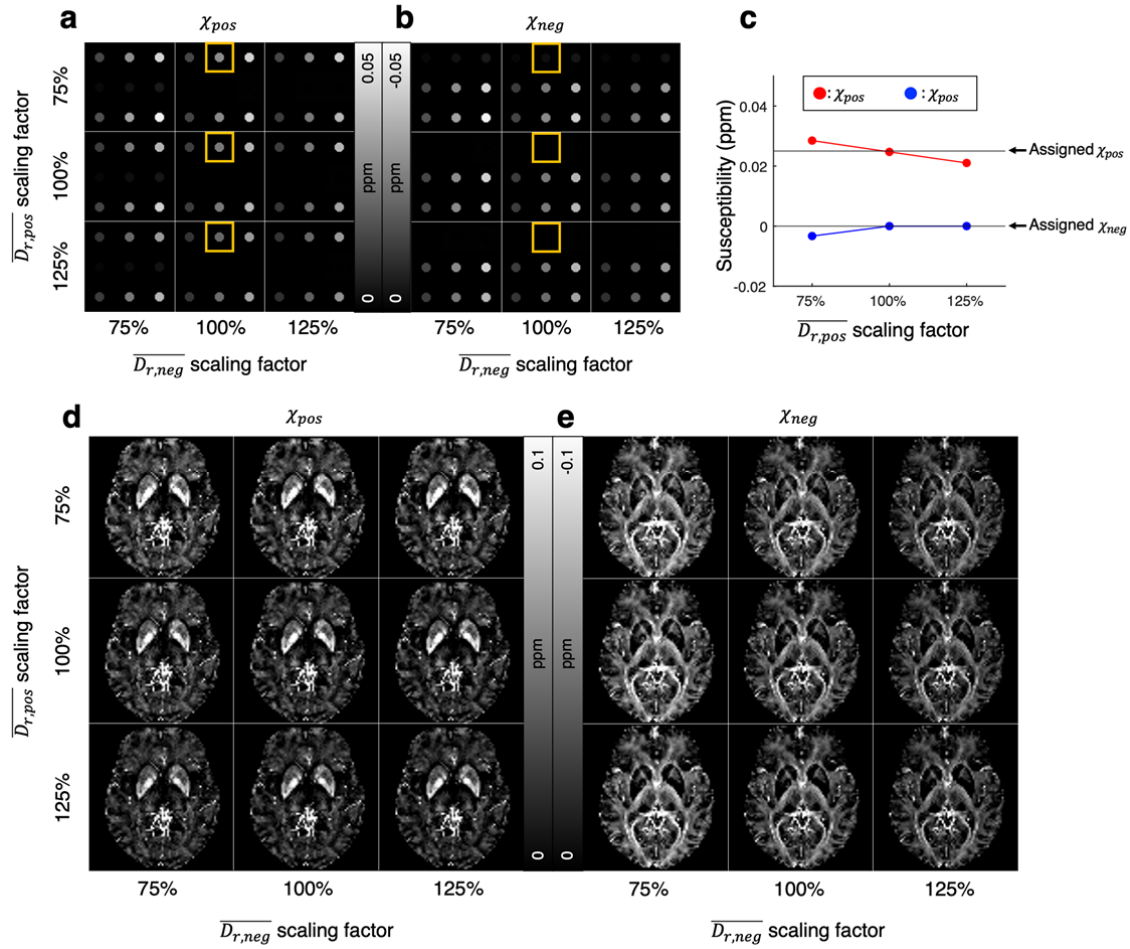
Supplementary Figure 7. Positive susceptibility measurements from χ -separation (red dots) and the susceptibility measurements from the conventional QSM (black dots) in ten ROIs: thalamus (Tha), caudate nucleus (CN), putamen (Put), substantia nigra (SN), globus pallidus (GP), red nucleus (RN), and four regions in white matter (genu and splenium of corpus callosum (CC), occipital WM (oWM), temporal WM (tWM), and frontal WM (fWM); dashed box). When the ROI-averaged susceptibility measurements are plotted with respect to the literature values of iron concentrations (gray matter iron concentrations from Schweser et al.⁵; white matter iron concentrations from Langkammer et al.⁶), the positive susceptibility results from χ -separation show a stronger linear relationship ($R^2 = 0.83$; red dashed line) than those from the conventional QSM ($R^2 = 0.73$; black solid line). Vertical error bars indicate the inter-subject standard deviations of the susceptibility values, whereas horizontal error bars denote the standard deviations of the iron concentrations from the literatures.



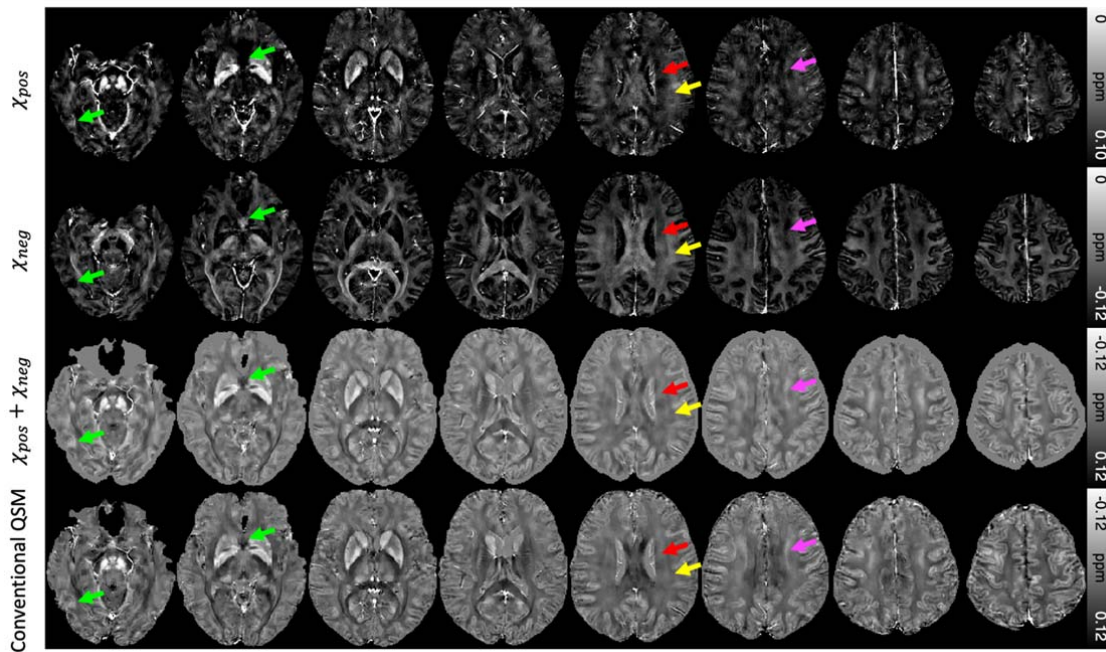
158

159 **Supplementary Figure 8. Estimation of the relaxometric constant in the *in-vivo* brains.** A
 160 linear regression between R_2' and conventional QSM values in the selected ROIs (Put, CN,
 161 RN, SN, and GP) reports the slope (i.e., $\overline{D_{r,pos}}$) of 137 Hz/ppm with R^2 of 0.70. Horizontal
 162 and vertical error bars indicate the inter-subject standard deviation of the susceptibility and
 163 R_2' values in each ROI.

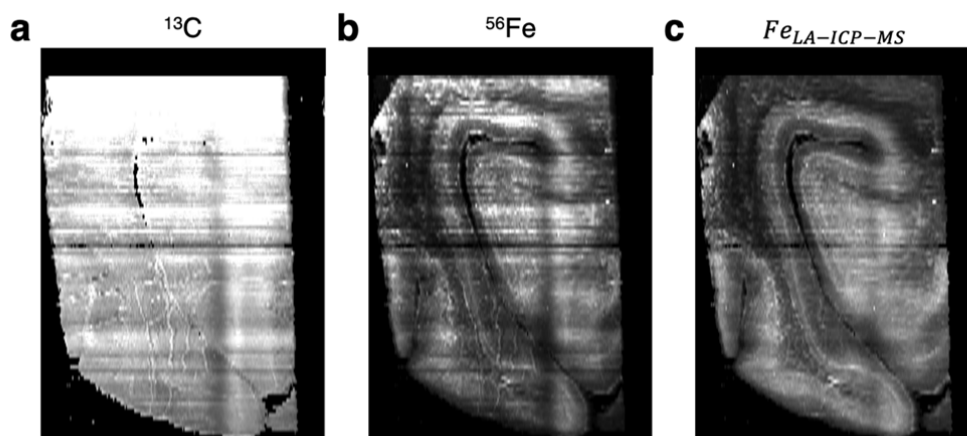
164



Supplementary Figure 9. Effects of the relaxometric constants on (a-c) the Monte-Carlo simulation and (d-e) the *in-vivo* experiment. When the positive and negative relaxometric constants were scaled between 75% to 125% of the original relaxometric constants, the positive and negative susceptibility maps show qualitatively similar contrasts, demonstrating the robustness of the χ -separation method for the range of errors in the relaxometric constants (a-b, d-e). The quantitative results from the cylinders in the yellow boxes (a-b) reveal the relationship between relaxometric constants and susceptibility estimation errors (c).



Supplementary Figure 10. Representative slices of the *in-vivo* χ -separation results. First, second, and third rows display the positive susceptibility map, the negative susceptibility map, and the sum of the two maps, respectively. The last row shows the conventional QSM map. Green arrows denote artifacts from large B_0 field inhomogeneity. Red arrows indicate fibers of corona radiata that are largely parallel to the B_0 field, whereas yellow arrows point superior longitudinal fasciculus fibers that are approximately perpendicular to the B_0 field. The contrast difference between these two areas may be related not only to myelin concentration difference and but also to fiber orientation-dependent anisotropic susceptibility^{7,8}. Pink arrows indicate streaking artifacts induced from ventricular cerebrospinal fluid and deep gray matter, which have been observed in conventional QSM results (see coronal image from MEDI in Figure 2 of Yoon et al.⁹).



187

188 **Supplementary Figure 11. Original LA-ICP-MS images of (a) ^{13}C and (b) ^{56}Fe , and (c)**
 189 **normalized ^{56}Fe image by ^{13}C .** Because of the long scan time of the LA-ICP-MS imaging
 190 (~ 7 hours), the ^{13}C image was utilized to remove the signal drifts of LA-ICP-MS in the ^{56}Fe
 191 image. The normalization may affect iron quantification¹⁰.

192

193 **SUPPLEMENTARY NOTE**

194 In this section, an analytical equation is derived to extend the linear relationship between
195 R_2' and bulk susceptibility in Eq. 3⁴ from susceptibility sources with a single source property
196 (i.e., single characteristic frequency and geometry) to susceptibility sources with multiple
197 source properties (i.e., K categories of the characteristic frequencies and/or geometries). The
198 derivation is demonstrated for a spherical source geometry but can be extended for other
199 geometries.

200 The notations for the following mathematical formula are listed below:

V_0 : volume of the medium

v_n : volume of the n^{th} susceptibility source

v : volume of the total susceptibility sources

V : total volume including the sources and medium ($= v + V_0$)

ς : volume fraction of the sources ($= \frac{v}{V}$)

201 ς_k : volume fraction of the sources in k^{th} category

χ_0 : susceptibility of the medium

$\hat{\chi}_k$: susceptibility of the source in k^{th} category

$\overline{\chi_k}$: bulk susceptibility of the source in k^{th} category relative to the medium

($= (\hat{\chi}_k - \chi_0) \cdot \varsigma_k$)

N : total number of the sources

N_k : number of the sources in k^{th} category

B_0 : applied magnetic field

M_0 : magnetization density of the medium ($= \chi_0 \cdot B_0$)

M_k : magnetization density of the source in k^{th} category ($= \hat{\chi}_k \cdot B_0$)

b_n : magnetic field perturbed by n^{th} source

b_0 : magnetic field in the medium in the absence of the source ($= B_0 - \frac{8\pi}{3} \cdot M_0$)

$\omega(\vec{r})$: frequency of the medium at point \vec{r}

$\omega_n(\vec{r})$: frequency of the medium at point \vec{r} generated by n^{th} source

ω_0 : reference frequency ($= \gamma \cdot b_0$)

$\delta\omega_{s,k}$: characteristic frequency of the spherical source in k^{th} category

$$(\gamma \cdot \frac{4\pi}{3} \cdot (M_k - M_0))$$

R_n : radius of n^{th} source

ϑ : angle relative to B_0

202 ρ : spin density of the medium

203 $P_k(R)$: probability distribution of the radius of the source in k^{th} category

204 All units are in CGS

205

206 In the presence of the susceptibility sources, the MRI signal from the medium is
207 calculated as a volume integral of spin magnetizations, which experience frequency shifts
208 from the susceptibility sources:

$$209 \quad S(t) = \frac{1}{V} \cdot \rho \int_{V_0} d\vec{r} \cdot \exp(-i \cdot \omega(\vec{r}) \cdot t) \quad [\text{Eq. S1}]$$

210 where

$$211 \quad \omega(\vec{r}) = \omega_0 + \sum_{n=1}^N \omega_n(\vec{r} - \vec{r}_n), \quad [\text{Eq. S2}]$$

$$212 \quad \omega_n(\vec{r} - \vec{r}_n) = \gamma \cdot b_n(\vec{r} - \vec{r}_n). \quad [\text{Eq. S3}]$$

213 Since we assumed spherical susceptibility sources,

$$\omega_n(\vec{r}) = \delta\omega_{s,k_n} \cdot \left(\frac{R_n}{|\vec{r}|}\right)^3 (3\cos^2\vartheta - 1) \quad [\text{Eq. S4}]$$

where k_n denotes the category where the n^{th} source is included ($k_n \in \{1, 2, \dots, K\}$).

When the sources are randomly distributed, the signal in Eq. S1 can be statistically averaged as follows:

$$\bar{S}(t) = \rho \cdot (1 - \varsigma) \cdot \prod_{n=1}^N \frac{1}{V - v_n} \cdot \int_{V - v_n} d\vec{r} \cdot \exp(-i \cdot \omega_n(\vec{r}) \cdot t). \quad [\text{Eq. S5}]$$

In this equation, the field perturbation effects of the N individual susceptibility sources are separated as a multiplication form. By substituting Eq. S4 into Eq. S5 and introducing the source radius R as a random variable, Eq. S5 becomes

$$\bar{S}(t) = \rho \cdot (1 - \varsigma) \cdot \prod_{n=1}^N \int dR \cdot P_{k_n}(R) \cdot \frac{1}{V - v(R)} \cdot \int_{r>R} d\vec{r} \cdot \exp\left(-i \cdot \delta\omega_{s,k_n} \cdot t \cdot \left(\frac{R}{r}\right)^3 (3\cos^2\vartheta - 1)\right). \quad [\text{Eq. S6}]$$

When N_k number of sources are included in the k^{th} category ($k \in \{1, 2, \dots, K\}$), Eq. S6 can be reformulated as follows:

$$\bar{S}(t) = \rho \cdot (1 - \varsigma) \cdot \prod_{k=1}^K \left\{ \int dR \cdot P_k(R) \cdot \frac{1}{V - v(R)} \cdot \int_{r>R} d\vec{r} \cdot \exp\left(-i \cdot \delta\omega_{s,k} \cdot t \cdot \left(\frac{R}{r}\right)^3 (3\cos^2\vartheta - 1)\right) \right\}^{N_k} \quad [\text{Eq. S7}]$$

This equation can be simplified as follows (see Appendix in Yablonskiy and Haacke⁴):

$$|\bar{S}(t)| = \rho \cdot (1 - \varsigma) \cdot \prod_{k=1}^K \left(1 - \frac{\varsigma_k}{N_k} \cdot \frac{2 \cdot \pi}{3 \cdot \sqrt{3}} \cdot |\delta\omega_{s,k}| \cdot t\right)^{N_k} \quad [\text{Eq. S8}]$$

assuming $|\delta\omega_{s,k}| \cdot t \gg 1$ for all k . This assumption is valid for ferritin particles at 3 T ($\delta\omega_s > 10^5$ Hz) for a typical echo time (> 1 ms).

Considering a large number of sources for all categories (i.e., $N_k \rightarrow \infty$ for all k), Eq. S8 is simplified as an exponential function:

$$|\bar{S}(t)| = \rho \cdot (1 - \varsigma) \cdot \exp \left[-\frac{2 \cdot \pi}{3 \cdot \sqrt{3}} \cdot \left(\sum_{k=1}^K |\delta \omega_{s,k}| \cdot \varsigma_k \right) \cdot t \right]. \quad [\text{Eq. S9}]$$

Using the definition, we can substitute $|\delta \omega_{s,k}| \cdot \varsigma_k$ as $\gamma \cdot \frac{4}{3} \cdot \pi \cdot |\hat{\chi}_k - \chi_0| \cdot B_0 \cdot \varsigma_k = \frac{4}{3} \cdot \pi \cdot \gamma \cdot B_0 \cdot |\overline{\chi}_k|$. Finally, the exponential decay constant in Eq. S9, which is equivalent to a R_2' relaxation rate, is represented as follows:

$$\sum_{k=1}^K \frac{2 \cdot \pi}{9 \cdot \sqrt{3}} \cdot \gamma \cdot B_0 \cdot |4 \cdot \pi \cdot \overline{\chi}_k| = \sum_{k=1}^K \frac{2 \cdot \pi}{9 \cdot \sqrt{3}} \cdot \gamma \cdot B_0 \cdot |\overline{\chi}_{k,SI}| = \sum_{k=1}^K D_{r,k} \cdot |\overline{\chi}_{k,SI}| = R_2'. \quad [\text{Eq. S10}]$$

where $\overline{\chi}_{k,SI}$ is equivalent to the bulk susceptibility value in the SI unit and $D_{r,k}$ is the relaxometric constant that describes the contribution of the bulk susceptibility of the k^{th} category source to R_2' . This result demonstrates that R_2' is proportional to the absolute sum of the bulk susceptibility values of the individual category.

For two categories of the susceptibility sources (i.e., $K = 2$) with the opposite sign (i.e., $\delta \omega_{s,1} > 0$, and $\delta \omega_{s,2} < 0$), Eq. S10 is simplified to Eq. 4, explaining the effects of positive and negative sources on R_2' . The relaxometric constant can be affected by water diffusion, and the size, geometry, and characteristic frequency of the susceptibility sources¹¹.

REFERENCES

1. Liu, T. et al. Morphology enabled dipole inversion (MEDI) from a single-angle acquisition: Comparison with COSMOS in human brain imaging. *Magnet Reson Med* 66, 777–783 (2011).
2. Liu, Z., Spincemaille, P., Yao, Y., Zhang, Y. & Wang, Y. MEDI+0: Morphology enabled dipole inversion with automatic uniform cerebrospinal fluid zero reference for quantitative susceptibility mapping. *Magnet Reson Med* 79, 2795–2803 (2018).
3. Ruh, A., Scherer, H. & Kiselev, V. G. The Larmor frequency shift in magnetically heterogeneous media depends on their mesoscopic structure. *Magnetic Resonance in Medicine* 79, (2018).
4. Yablonskiy, D. A. & Haacke, E. M. Theory of NMR signal behavior in magnetically inhomogeneous tissues: The static dephasing regime. *Magnet Reson Med* 32, 749–763 (1994).
5. Schweser, F., Deistung, A., Lehr, B. W. & Reichenbach, J. R. Quantitative imaging of intrinsic magnetic tissue properties using MRI signal phase: an approach to in vivo brain iron metabolism? *Neuroimage* 54, 2789–2807 (2011).
6. Langkammer, C. et al. Quantitative susceptibility mapping (QSM) as a means to measure brain iron? A post mortem validation study. *Neuroimage* 62, 1593–1599 (2012).
7. Lee, J. et al. Sensitivity of MRI resonance frequency to the orientation of brain tissue microstructure. *P Natl Acad Sci Usa* 107, 5130–5 (2010).
8. Wharton, S. & Bowtell, R. Fiber orientation-dependent white matter contrast in gradient echo MRI. *Proc National Acad Sci* 109, 18559–18564 (2012).
9. Yoon, J. et al. Quantitative susceptibility mapping using deep neural network: QSMnet. *Neuroimage* 179, 199–206 (2018).
10. Bulk, M. et al. Quantitative MRI and laser ablation-inductively coupled plasma-mass spectrometry imaging of iron in the frontal cortex of healthy controls and Alzheimer's disease patients. *Neuroimage* 215, 116808 (2020).
11. Yung, K.-T. Empirical models of transverse relaxation for spherical magnetic perturbers. *Magn Reson Imaging* 21, 451–463 (2003).